

Testing magnetically confined wind shock models for β Cep using XMM-Newton and Chandra phase-resolved X-ray observations

F. Favata¹, C. Neiner², P. Testa³, G. Hussain⁴, and J. Sanz-Forcada⁵

¹ European Space Agency, 8-10 rue Mario Nikis, 75015 Paris, France
e-mail: Fabio.Favata@esa.int

² GEPI, UMR 8111 du CNRS, 5 place Jules Janssen, 92195 Meudon Cedex, France

³ Kavli Institute for Astrophysics and Space Research, MIT, Cambridge, Mass., USA

⁴ European Southern Observatory, Garching bei Munchen, Germany

⁵ Laboratorio de Astrofísica Espacial y Física Fundamental, INTA, PO Box 50727, 28080 Madrid, Spain

Received ; accepted

ABSTRACT

Aims. We have performed a set of high- and low-spectral resolution phase-resolved X-ray observations of the magnetic B star β Cep, for which theoretical models predict the presence of a confined wind emitting X-rays from stationary shocks. Some of the models predict, given the peculiar geometry of β Cep, strong rotational modulation of the X-ray emission, while other models predict a much lower amplitude modulation at 90 deg phase shift from the modulation predicted from the first group of models. Our observations were designed to provide a stringent test of such models.

Methods. We obtained four observations spaced in rotational phase with XMM-Newton (using both the EPIC cameras and the RGS spectrograph) and with Chandra (using the LETG spectrograph). A detailed analysis of the data was performed to derive both photometric and spectral parameters from the EPIC data, searching for rotational modulation, and to derive the location of the X-ray plasma from the line ratios in the He-like triplets of N, O and Ne from the RGS data. The LETG data were used to constrain the presence of bulk motions in the plasma.

Results. The strong rotational modulation predicted by the early, static magnetically confined wind model for the X-ray emission is not observed in β Cep. The small modulation present goes in the opposite direction, pointing to the absence of any optically thick disk of neutral material, and showing a modulation consistent with the later, dynamic models of magnetically confined wind models in B stars. The lack of observed bulk motion points to the plasma being confined by a magnetic field, but the low plasma temperature and lack of any flaring show that the plasma is not heated by magnetic reconnection. Therefore, the observations point to X-ray emission from shocks in a magnetically confined wind, with no evidence of an optically thick, dense disk at the magnetic equator.

1. Introduction

Early-type stars were established as strong soft X-ray sources already during the very first survey of stellar X-ray emission conducted with the *Einstein* observatory (Vaiana et al., 1981). O and B stars lack the external convection layer which is an essential component of the dynamo in late-type dwarfs, and thus are expected to lack the highly structured magnetic fields which confine and heat solar-type coronae. The observed X-ray emission is thermal in nature, and in general of lower temperature than observed in active late-type stars. The mechanism initially proposed to explain the observed X-ray emission was self shocking in the radiatively driven fast, strong stellar winds which are a characteristic of massive stars (Lucy & White, 1980). This scenario makes a well-defined prediction, i.e. that emission lines should be broad and blue-shifted. The advent

high spectral resolution made possible by the launch of XMM-Newton and Chandra has shown that some massive stars do indeed show the expected signature of X-ray emission from the wind (e.g. ζ Pup, Cassinelli et al., 2001). Other stars however show narrow spectral lines (e.g. θ^1 Ori C, Gagné et al., 2005). Narrow lines imply a low-velocity plasma which has been interpreted as a confined plasma, likely requiring magnetic fields (e.g. Schulz et al., 2003, Schulz et al., 2006 and reference therein). Alternative scenarios not requiring magnetic confinement for the X-ray emission from early-type stars showing narrow lines have also been put forward (Cohen et al., 2006; Leutenegger et al., 2006). A recent survey of early-type high-resolution spectra has been performed by Waldron & Cassinelli (2007).

Recently, dipolar fields have been detected in a number of massive stars, in some cases with the magnetic axis at a significant angle from the rotation axis. Scenarios implying magnetic

confinement of the wind from a dipolar magnetic field have been developed, and (as discussed below) they succeed in explaining several of the observed characteristics in massive stars with a measured magnetic fields and X-ray emission. For example, Babel & Montmerle (1997a) developed a magnetically confined wind shock model (MCWS) to explain the characteristics of the X-ray emission from Ap and Bp stars, and Babel & Montmerle (1997b) applied the MCWS model to explain some of the salient characteristics of the X-ray emission of θ^1 Ori C, one of the only two O-type stars with a detected magnetic field. θ^1 Ori C shows strong modulation of the X-ray emission with the rotational period, with a nearly sinusoidal light curve and a $\approx 50\%$ peak-to-peak modulation amplitude (Gagne et al., 1997; Stelzer et al., 2005); such strong modulation agrees very well with the predictions of the MCWS scenario. Interestingly, the other O star on which a magnetic field has recently been detected, HD 191612 (Donati et al., 2006) has an unusually slow rotation rate, and it also has a field with a strong dipolar component.

As discussed in Sect. 2, β Cep has a significant dipolar magnetic field (≈ 360 G, Henrichs et al., 2000), with the magnetic axis at almost 90 deg from the rotational axis, and it therefore is a particularly interesting star for the study of the magnetically confined wind model. Its X-ray emission had already been detected by the *Einstein* observatory, and Donati et al. (2001) (hereafter D01) devised a detailed model for it, based on the MCWS scenario of Babel & Montmerle (1997b) and the later ROSAT observations. They make clear and verifiable predictions on the temporal variability of the X-ray emission and on its spectrum, as well as on the spatial location of the X-ray plasma.

Later work based on dynamical modeling of the wind-magnetic field interaction however showed that the thick disk predicted by Babel & Montmerle (1997b) would be unlikely to form around a star like β Cep (Gagné et al., 2005; ud-Doula & Owocki, 2002; Townsend & Owocki, 2005).

We have carried out a campaign of X-ray observations using both *Chandra* and *XMM-Newton*, specifically designed to provide a stringent test of MCWS-based model of the X-ray emission of β Cep. The observations were designed to determine whether the X-ray emission presents the variability with rotational phase predicted by the D01 model, and (by using triplet ratios and Doppler shifts) at which distance from the star's photosphere the bulk of the X-ray emission is concentrated. Our interest in the X-ray emission of β Cep was initially also driven by its being a Be star, although, as discussed in Sect. 2, recent observations have suggested that the Be phenomenology is due to the secondary (presumably much less X-ray active) companion in the β Cep system, rather than to the magnetic, X-ray active primary.

The present paper is structured as follows: after the Introduction, the characteristics of our target star, β Cep, are discussed in Sect. 2. *XMM-Newton* and *Chandra* observations are discussed in Sect. 3 with their analysis, and the relative results are presented in Sect. 4. Finally, our conclusions are presented in Sect. 5.

2. The star β Cep

β Cep stars are early-B subgiants or giants that exhibit coherent short-period radial velocity variations, successfully explained in terms of pulsations with periods ranging from about 3 to 8 hours. The driving mechanism of pulsation in β Cep stars is the κ mechanism, i.e. an effect of the changing opacity of iron-peak elements deep in the stellar envelope (Dziembowski & Pamiatnykh, 1993).

The prototype of this class, the star β Cep itself (HD 205021, HR 8238), long classified as a B1IIIe star, is at a Hipparcos distance of 182 pc. The literature values of the basic photospheric parameters of β Cep span a relatively wide range: T_{eff} varies from 24 000 K (e.g. Heynderickx et al., 1994) to 27 000 K (e.g. Tian et al., 2003), $\log g$ from 3.31 (e.g. Heynderickx et al., 1994) to 4.07 (e.g. Cugier & Boratyn, 1992), while M ranges from $9.9M_{\odot}$ (D01) to $16.4M_{\odot}$ (Heynderickx et al., 1994). The radius R has been estimated from $6.5R_{\odot}$ (D01) to $8.6R_{\odot}$ (Hutchings & Hill, 1977). The main pulsation period of β Cep, 4 hours and 34 minutes, corresponds to a radial p mode, but additional periods exist due to non-radial modes. While Daszyńska-Daszkiewicz & Niemczura (2005) and Niemczura & Daszyńska-Daszkiewicz (2005) derive a photospheric metal abundance very close to solar ($m/H = -0.07 \pm 0.10$) from the analysis of IUE spectra, Morel et al. (2006) recently performed a detailed abundance analysis of the photosphere of β Cep based on high-resolution optical spectra, deriving abundances significantly lower than solar values, except for N and possibly S, as detailed in Table 1. In the following we adopt the abundances of Morel et al. (2006).

Table 1. The photospheric abundances of β Cep as determined by Morel et al. (2006). The first column gives the ratio between the photospheric abundance of β Cep and the standard photospheric abundance of the Sun of Grevesse & Sauval (1998). The second column gives the abundance relative to the solar abundances recently determined using 3D calculations by Asplund et al. (2005). The relative 1σ errors are given in column 3.

	$M/M_{\odot D}$	$M/M_{\odot 3D}$	1σ (dex)
C	0.32	0.43	0.10
N	0.98	1.35	0.13
O	0.44	0.65	0.14
Mg	0.54	0.60	0.21
Al	0.36	0.45	0.16
Si	0.36	0.40	0.23
S	0.65	1.00	0.37
Fe	0.55	0.62	0.23

β Cep is the primary star of a triple system. The visual companion ADS 15032 B, is a $V = 7.9$ A2.5V star located at 13.4 arcsec from the primary. It has an orbital period of about 91.6 yr and was at periastron in 2006 (Pigulski & Boratyn, 1992). The third component of the system, a physical companion, is a $V = 6.6$ B6-8 star situated at 0.1 arcsec from the primary

(Schnerr et al., 2006), detected through speckle interferometry (Gezari et al., 1972).

The β Cep system also exhibits emission in its Balmer lines, so that the primary itself has long been considered as a Be star. In Be stars the Balmer emission is due to the presence of circumstellar matter ejected by the star. The Be character is usually variable with time, and the β Cep system is no exception. The time evolution of the intensity of its $H\alpha$ emission line is shown in Fig. 1: major outbursts occurred around 1990 and 2001. At the time of our X-ray observations in 2005 (see Fig. 1), the $H\alpha$ emission was decreasing but still visible in the line profile. However, Be stars usually rotate fast, at about $v \sin i = 250 \text{ km s}^{-1}$ on average, while the β Cep primary rotates intrinsically slowly, at $v \sin i = 20 \text{ km s}^{-1}$, and $i = 60 \text{ deg}$ (Abt et al., 2002), making it different from classical Be stars.

The conundrum relative to the unusually low rotation speed of β Cep relative to its Be status has apparently been recently solved by Schnerr et al. (2006), who argue that the $H\alpha$ emission does not come from the bright primary, but rather from the fainter speckle companion. This would make the β Cep primary a normal B star, rather than a peculiar Be one.

The rotational period of β Cep is almost exactly 12 days, and in the present study we use the ephemeris of D01,

$$JD = 2\,451\,238.15 + N \times 12.00092 \quad (1)$$

where phase 0 is the phase at which the longitudinal magnetic field (see below) is at maximum. This ephemeris is consistent, within the error bars, with the values published by Henrichs et al. (2000) and Henrichs et al. (2005).

2.1. The magnetic field of β Cep

Over the past decade magnetic fields have been detected in an increasing number of normal massive stars, in addition to the well known fields of Ap/Bp stars. In particular magnetic fields have been discovered in a few β Cep stars including β Cep itself (Henrichs et al., 2000). The longitudinal magnetic field of β Cep is observed to vary with the 12 day rotation period.

These observations of magnetic massive stars can usually be explained with the magnetic oblique rotator model (Stibbs, 1950). In this model, the magnetic field structure is not symmetric about the rotation axis of the star. For the simplest case of a dipole field, this means that the axis of the dipole and the axis of rotation of the star do not coincide. The observed geometrical configuration can then be characterized by the inclination angle i between the observer's line-of-sight and the stellar rotation axis, and by the obliquity angle β between the magnetic axis and the rotation axis. In the case of a dipolar magnetic star, as the star rotates, the aspect of its visible hemisphere changes. This leads to variations in a number of observables with the stellar rotation period. β Cep hosts such a magnetic oblique dipole field with an inclination angle $i = 60^\circ$ and its rotation and magnetic axis almost perpendicular ($\beta = 85^\circ$). Therefore, as the star rotates, the observer successively sees the magnetic equator nearly edge-on or face-on. Fig. 2 shows the magnetic oblique dipole model of β Cep at different rotational phases, with the magnetic equator drawn as a thicker black line.

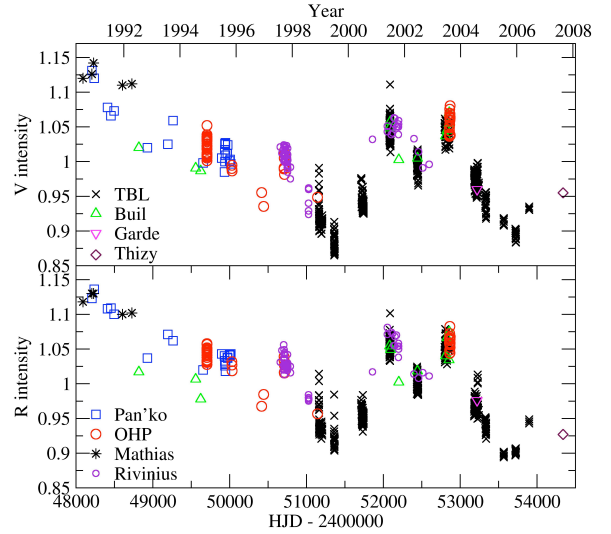


Fig. 1. Evolution of the intensity of the Halpha emission of beta Cep with time. Data have been obtained at Telescope Bernard Lyot (TBL) of Pic du Midi Observatory and Observatoire de Haute-Provence (OHP), and collected from the litterature (Pan'ko & Tarasov, 1997), amateurs astronomers (C. Buil, O. Garde, T. Thizy) and private communications (P. Mathias, T. Rivinius).

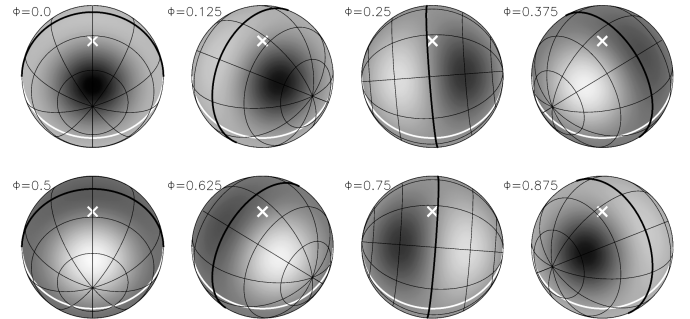


Fig. 2. Greyscale representation of the relative contribution of the magnetic dipole to the integrated longitudinal magnetic field on the visible hemisphere of β Cep, at different rotational phases, with step $\delta\Phi = 0.125$. Phase 0 is the phase at which the longitudinal field is at maximum, as in the ephemeris above. The black color corresponds to positive field values and the white color to negative field values. A grid of magnetic longitudes and latitudes is overplotted, with the magnetic equator shown as a thicker black line. The rotation axis and equator are shown with a white cross and line respectively. Although the strongest magnetic field is at the magnetic poles, the positions on the stellar surface that contribute the most to the longitudinal field are not at the poles, due to a geometrical effect and to the limb darkening effect.

In the presence of a sufficiently strong dipolar magnetic field, the stellar wind escapes from the star via its magnetic

poles and follows the magnetic field lines. As the star rotates one thus observes a variation of the equivalent width of the wind-sensitive lines such as the UV resonance lines of highly ionized species. Such variations have been observed in β Cep, by Henrichs et al. (2000), who find that the C iv line is strongly modulated with the rotation period of 12 d, maintaining phase coherence over several years. This shows that the transition-region temperature material responsible for the emission in C iv is magnetically confined (and, incidentally, that it is associated with the primary, rather than with the Be secondary).

If the magnetic field is strong enough the wind can be fully magnetically confined in a region close to the star (Babel & Montmerle, 1997b). In this case the stellar wind particles coming from both magnetic poles, forced to follow the magnetic field lines, collide at the magnetic equator creating a deceleration disk or circumstellar clouds. The MCWS model has been successfully applied to explain the characteristics of the X-ray emission in a number of massive stars, in particular θ^1 Ori C (Donati et al., 2002; Gagné et al., 2005). D01 showed that the MCWS seems to also apply for β Cep. It explains at the same time the rotation modulation observed in the wind-sensitive UV lines and in the longitudinal field measurements.

2.2. The X-ray emission of β Cep

As mentioned above, stars hotter than B4 have sufficiently strong winds to give rise to X-ray emission in wind shocks. However, in the case of magnetically confined winds, shocks may also take place at the stellar equator, where the winds originating from the two magnetic poles collides. The resulting shock is expected to produce X-ray emission localized at or close to the magnetic equator.

β Cep has been known to be an X-ray source since its observation with *Einstein*. The X-ray spectrum, derived from ROSAT All Sky Survey observations obtained in 1990 and reported by Berghoefer et al. (1996), has been interpreted as originating from a thermal source with an X-ray temperature of 0.24 keV and an X-ray luminosity of 6.5×10^{29} erg/s, for an assumed distance of 71 pc. Rescaling the reported X-ray luminosity to the Hipparcos distance of 182 pc, one obtains $L_X = 4.2 \times 10^{30}$ erg/sec. Agrawal et al. (1984) had obtained $L_X = 9.1 \times 10^{30}$ erg/sec, from data obtained with the IPC on-board *Einstein*, assuming a distance of 263 pc. Again rescaling this X-ray luminosity to the Hipparcos distance of 182 pc, one obtains $L_X = 4.3 \times 10^{30}$ erg/sec, which is very close to the value derived above from ROSAT data.

Cohen (2000) claim the detection of a 7% modulation in the X-ray emission of β Cep at the 4.57 hrs pulsation period, based on analysis of the ROSAT All Sky Survey data.

The MCWS by Babel & Montmerle (1997b) makes clear predictions about the characteristics of the X-ray emission from β Cep, as extensively discussed in Sect. 4.2 of D01. The luminosity, temperature distribution and emission measure predicted by the plasma distribution of this model are, in the 0.1–2.0 keV range of the ROSAT PSPC, 7.2×10^{30} erg/sec, 3.2 MK and 4.5×10^{33} cm⁻³ for the X-ray luminosity, temperature and

emission measure respectively. These are in good agreement with the ROSAT observation (Berghoefer et al., 1996).

Moreover, the same model makes an easily testable prediction regarding the temporal variability of the X-ray emission, for which strong modulation as a function of rotational phase is expected. The X-ray emission is produced on the shocks located on both sides of the cooling disk, whose density is sufficiently high to make it completely opaque to the X-rays emitted by the shock. As a consequence, when the system is viewed with the disk edge-on, X-rays will reach the observer from both shocks (on the magnetic north and south side of the disk), whereas when the disk is seen face-on, only one of the shocks will be visible in X-rays. The expected X-ray modulation amplitude in the MCWS scenario of D01 is thus of the order of 50%, although (as discussed by D01) the predicted shape of the X-ray light curve can be strongly affected by the disk's characteristics, for example its warp.

The later, dynamical models of ud-Doula & Owocki (2002) and Gagné et al. (2005), when applied to β Cep, make a very different prediction regarding the modulation of its X-ray emission: in particular, the magnetic confinement parameter

$$\eta_* = \frac{B_*^2(\pi/2)R_*^2}{\dot{M}v_\infty} \quad (2)$$

using the appropriate values for β Cep ($B = 360$ G, $R_* = 6.5 R_\odot$, $\dot{M} = 10^{-9} M_\odot \text{ yr}^{-1}$, $v_\infty = 800\text{--}1500$ km s⁻¹) would be high ($\eta_* \simeq 1000$), so that the Gagné et al. (2005) model predicts that the magnetosphere would be rigid out to the Alfvén radius ($R_A \simeq 5 R_*$) and the X-ray shocks would form just outside the Alfvén radius but inside the Kepler radius $R_K = 7 R_*$ (M. Gagné, private communication). This implies a small modulation of the X-ray activity, at the $\simeq 5\%$ level, with a minimum when the star is seen magnetic equator on, i.e. with the opposite phase as the modulation predicted by the D01 model.

3. Observations

In the course of our campaign we have observed β Cep with both *Chandra* and *XMM-Newton*. In both cases the proposed observational strategy was to perform 4 observations, as close as possible to phases 0.0, 0.25, 0.50 and 0.75. Phases 0.0 and 0.50 correspond to the magnetic equator seen face-on, while phases 0.25 and 0.75 correspond to the edge-on configuration. In the MCWS scenario, these 4 observations should ensure maximum modulation of the X-ray emission.

The *XMM-Newton* observatory allows simultaneous operation of the RGS high-resolution spectrograph and of the EPIC cameras. The goal of the *XMM-Newton* observation was to detect modulation in the spectral parameters, namely the global spectral temperature and emission measure as observed in the EPIC low-resolution CCD spectra, and in the triplet ratios from the RGS spectra. The triplet ratios, as discussed below, are a diagnostic, for early-type stars, of the distance at which the emitting plasma is located from the star.

The *Chandra* observation was performed using the LETGS spectrograph, with the aim of detecting whether the lines would be broadened asymmetrically (as e.g. expected in an unconfined,

self-shocked wind), or symmetrically (as expected if significant rotational broadening is present), or whether modulation of the radial velocity with the star’s rotational period is present (as expected e.g. in the presence of strongly localized plasma).

In practice, a number of constraints on the scheduling of space observatories made it difficult to schedule the observations exactly at the desired phases. The *Chandra* observations were particularly critical because of issues with the spacecraft thermal control, so that in practice the phase coverage is, specially for the *Chandra* data, not optimal – see Table 2 for the phase coverage of the XMM-*Newton* observations, and Table 6 for the *Chandra* observations.

3.1. XMM-Newton data reduction

Each of the 4 XMM-*Newton* observations was processed individually with the standard SAS V.6.0 pipeline. We have reduced and analyzed the RGS (1 and 2) data, as well as the EPIC MOS and pn data. We will report only the results obtained on the pn data, as these were consistent with the MOS data (with one exception noted in the text). Some periods of high background (proton flaring) were present in the observations, so that the EPIC data were screened to exclude them. We used as criterium the number of events detected at energies over 10 keV in the whole frame, and we discarded data periods in which this rate was greater than 12 per minute. The RGS1 and RGS2 spectra were analyzed separately, using the “PintOfAle” package (Kashyap & Drake, 2002) to determine the line fluxes.

Given the accuracy of the pointing, we found that it was possible to use the same source and background regions for all four observations.

3.2. Chandra data reduction

The *Chandra* data were reduced using the standard pipeline procedures in the latest release of the data reduction package, CIAO (v.3.3.0.1). Barycentric corrections were applied to the timing in the reduced files, accounting and correcting for the spacecraft motion. Background-subtracted spectra and lightcurves were extracted from four separate event files, one for each *Chandra* observation. X-ray lightcurves were created by defining source and background regions and dividing the background region count rate by the relevant scaling factor prior to background subtraction. The pointing stability of *Chandra* was also stable enough to enable the use of the same background and source regions for all four exposures.

Four sets of spectra were extracted, one for each of the four observations, integrating over the full exposure in each observation. As we wish to measure centroid positions accurately and individual lines have limited statistics, we sum the spectra from observations taken at similar phases (the first two data sets are centered near phase ~ 0 and the other 2 near phase 0.25). As the LETG wavelength scale is subject to non-linear deviations from the laboratory positions of the wavelengths (Chung et al., 2004), the +1 and –1 orders may show systematic differences. To ensure that we can distinguish between instrumental variability and genuine variability in the target system, we consider

the +1 and –1 orders separately in the subsequent analysis. We use the +1 and –1 order profiles to test for consistency and evaluate the precision of any shifts in centroid position measurements from one observation to another.

4. Results

4.1. EPIC data

We first inspected the background-subtracted light curves from the pn detector, shown in Fig. 3. Small amplitude variability is likely present in all 4 observations, with a formal Kolmogorov-Smirnov (KS) test showing a high probability of the source having undergone some actual variability during the 4th segment (bottom right panel of Fig. 3). On the other hand, during the 3rd segment of the observation (bottom left panel of Fig. 3), the KS test gives a very low probability of the source being variable, consistent with a lack of actual variations during the observation.

We also searched for evidence of modulation in the intensity of the X-ray emission at the 4h 34m pulsation period of β Cep, as reported by Cohen (2000). A period search performed on the complete pn data set using a χ^2 test on the phase-folded data set failed to detect any significant periodicity. In particular, no periodicity is evident at the 4h 34m pulsation period. Inspection of the 4 pn individual light-curves phase-folded at the pulsation period does not show any evidence of modulation in any of them. Furthermore, any possible hint of a modulation is at a different phase in each of the 4 light curves. This, jointly with the fact that Cohen (2000) have not performed a period search, but rather assumed the period and fitted the amplitude and phase, makes it likely that the period reported by Cohen (2000) is spurious.

We have fitted the 4 individual EPIC pn spectra with variable abundance thermal models. To obtain a satisfactory fit the spectra require two temperature components. The lower temperature component at $T \simeq 0.25$ keV is dominant, with an emission measure in all cases more than one order of magnitude larger than the one of the hotter temperature. The hotter temperature is not well constrained, due to the low statistics of the high-energy tail in the spectra, and it ranges between 0.7 and 2.0 keV. Abundances are also not strongly constrained, and appear to be, if anything, moderately depleted with respect to the photospheric abundances of β Cep. The best fit values reported in Table 2 show some evidence for variations of the abundance among the four spectra, in particular for Si. While the formal robustness of such fluctuations is modest, certainly the visual appearance of the pn spectra for the first and second observation (Fig. 4) is strikingly different, with the Si complex at $\simeq 1.9$ keV very prominent in the first observation and almost absent in the second one.

The level of photometric variability among the 4 observations is modest (of order 10%), allowing us to perform a joint spectral analysis of all four spectra simultaneously. The results are reported in Table 3. Given the availability of recently determined photospheric abundances for β Cep (Morel et al., 2006, see Table 1) we can determine the ratio of coronal to photospheric metallicity for β Cep itself, without reference to the

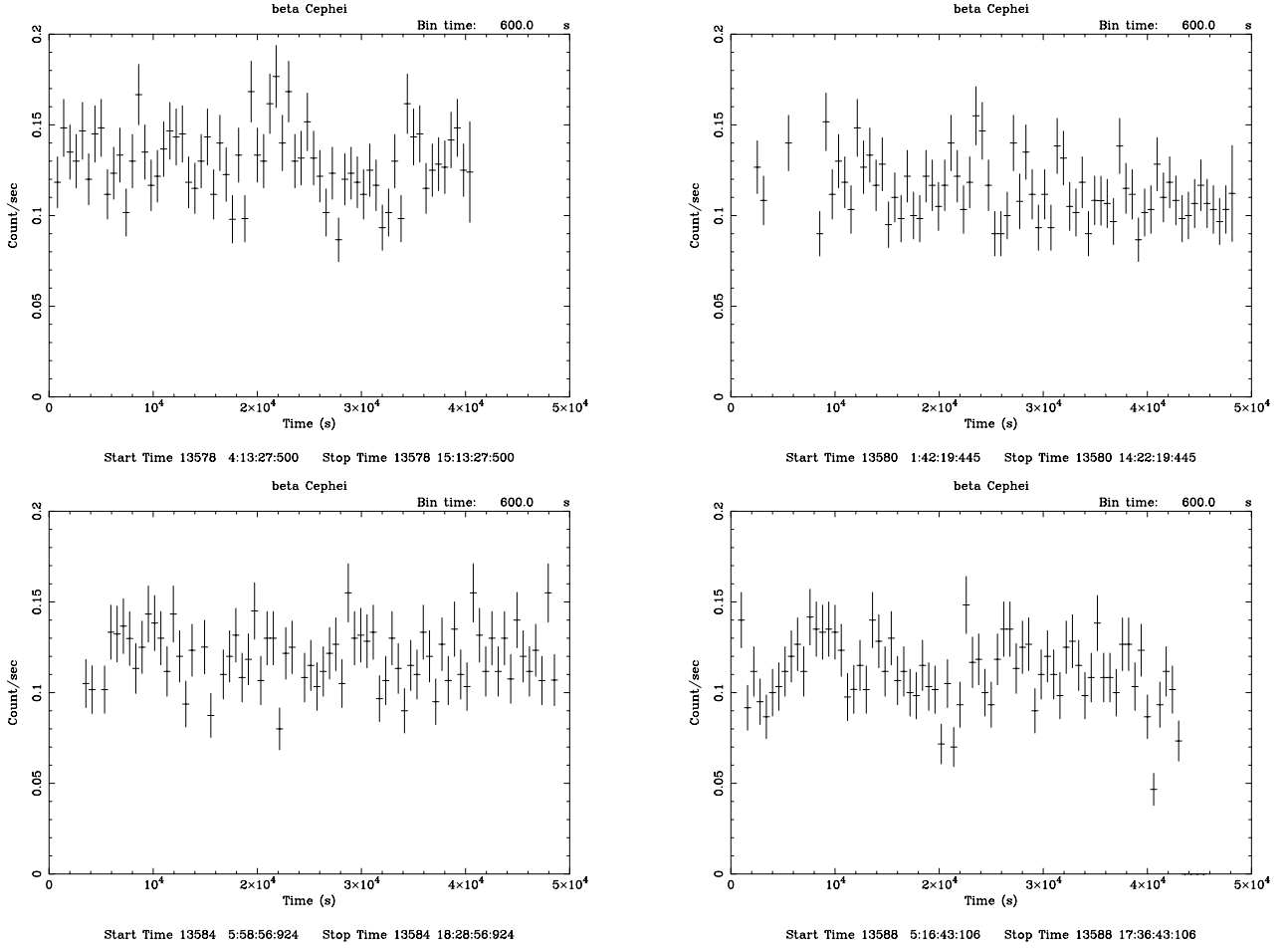


Fig. 3. The 4 light curves from the EPIC (pn) observations, background subtracted and binned at 1200 s resolution.

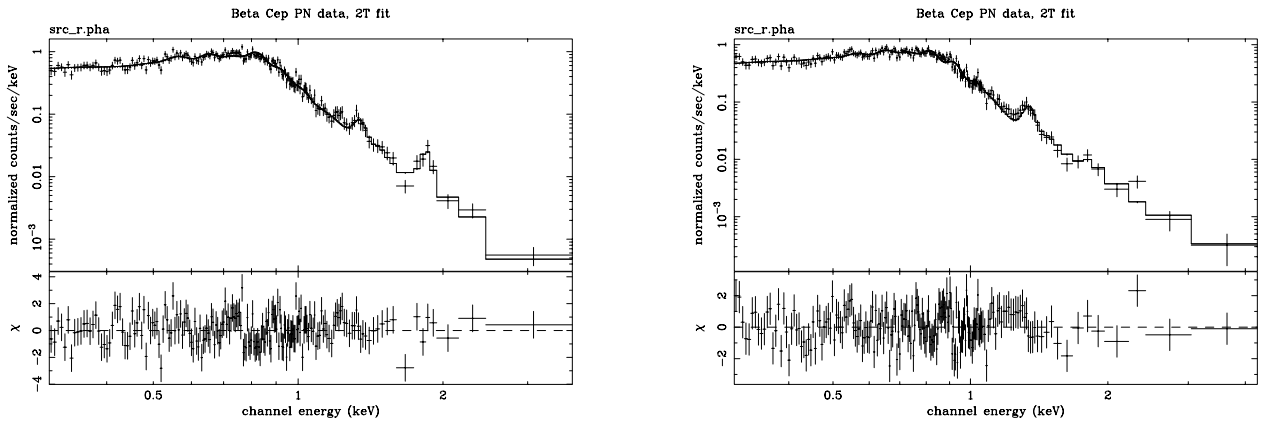


Fig. 4. Two-temperature, variable abundance fits to the EPIC pn spectra obtained in the first (left panel) and second (right panel) observations of β Cep. The relevant best fit parameters are presented in Table 2.

solar metallicity, as reported in Table 1. Only 3 elements (O, Si, Fe) have both coronal and photospheric abundances available, and again, moderate metal depletion in the X-ray emitting plasma with respect to the stellar photosphere is present.

The $N(H)$ resulting from the fit ($2.5 \times 10^{20} \text{ cm}^{-2}$) corresponds (using the relation $N(H)/A_V = 1.9 \times 10^{21}$) to an interstellar absorption of 0.13 mag. This is consistent with the published values for the interstellar reddening toward β Cep ($E_{B-V} \leq 0.04$, corresponding to $A_V \leq 0.13$).

In the ROSAT PSPC band (0.1–2.0 keV), the best-fitting model to the pn data has a flux corresponding to an X-ray luminosity of $4.0 \times 10^{30} \text{ erg/sec}$, showing very little long-term variability when compared to the 1990 ROSAT observation, which had an X-ray luminosity of $4.2 \times 10^{30} \text{ erg/sec}$.

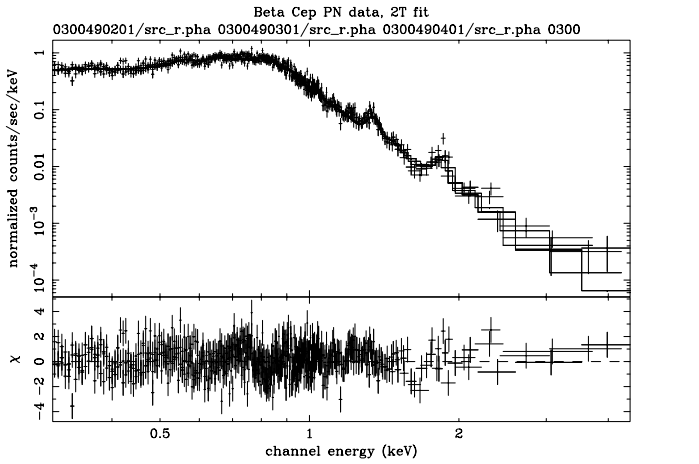


Fig. 5. Joint two-temperature, variable abundance fit to the 4 pn spectra of β Cep. The relevant best fit parameters are presented in Table 3.

4.2. RGS data

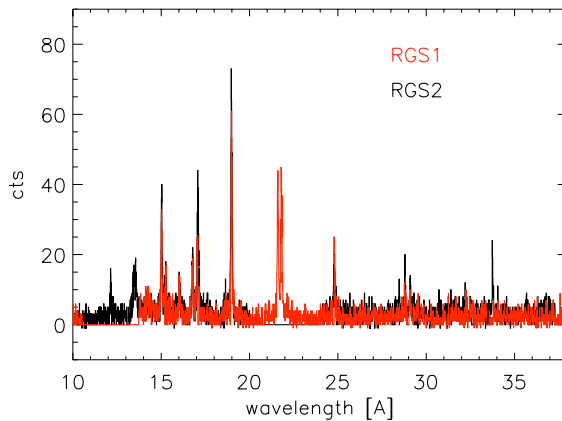


Fig. 6. The RGS1 (red) and RGS2 (black) spectra. All 4 individual spectra have been coadded in this plot.

Table 3. The joint best-fit spectral parameter for the 2- T fit with individually varying metal abundances for the 4 pn spectra. The notation “ M/M_{\odot} ” indicates the ratio between the β Cep coronal abundance and the solar photospheric abundance. The notation “ M/M_{phot} ” indicates the ratio between the coronal abundance of β Cep determined here and the photospheric abundance of β Cep determined by Morel et al. (2006). In all cases the solar photospheric abundances of Grevesse & Sauval (1998) have been used. The indicated uncertainties are 90% errors as resulting from a $\Delta\chi^2$ analysis. For all heavy elements not explicitly indicated, the abundances are equal to the value for Fe.

$N(H)$	$2.50 \pm 0.01 \times 10^{20} \text{ cm}^{-2}$
T_1	$0.24 \pm 0.01 \text{ keV}$
T_2	$0.63 \pm 0.03 \text{ keV}$
EM_1	$1.1 \pm 0.2 \times 10^{54} \text{ cm}^{-3}$
EM_2	$1.3 \pm 0.3 \times 10^{53} \text{ cm}^{-3}$
O/O_{\odot}	0.12 ± 0.02
Ne/Ne_{\odot}	0.18 ± 0.03
Si/Si_{\odot}	0.31 ± 0.06
Fe/Fe_{\odot}	0.33 ± 0.04
O/O_{phot}	0.28
Si/Si_{phot}	0.86
Fe/Fe_{phot}	0.60

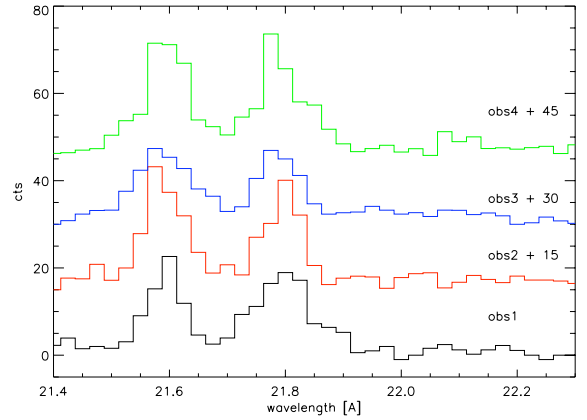


Fig. 7. The 4 individual RGS1+RGS2 spectra in the region of the O VII triplet. The spectra have been offset in the vertical direction for clarity.

We have first analyzed the 4 individual RGS spectra separately. As shown in Fig. 7 for the region of the O VII triplet, given the moderate statistics of the spectra no difference is visible among the different spectra. We have therefore coadded them and limited the further analysis to the coadded spectrum. The coadded spectrum is shown in Fig. 8, again limited to the O VII triplet region.

The RGS spectral range includes a number of He-like triplets which provide useful diagnostics of the plasma conditions. The most relevant at the plasma temperature of β Cep are the ones from N VI (at 29 Å), O VII (at 22 Å) and Ne IX (at 13.5 Å), each composed of 3 spectral features: the resonance line r ,

Table 2. The spectral parameters derived from the XMM-Newton EPIC pn observations, together with the relative phase coverage. The reported flux is measured in a 0.3-7.0 keV band.

Obs.	201	301	401	501
Start date	2005-07-27	2005-07-29	2005-08-02	2005-08-06
Start time (UT)	04:07:27	01:36:19	05:53:00	05:10:42
Obs. duration (s)	39 234	41 030	42 504	38 170
ϕ begin	0.03	0.19	0.54	0.87
ϕ end	0.07	0.23	0.58	0.91
$N(\text{H})$ (10^{20} cm^{-2})	4.5 ± 0.1	5.2 ± 0.2	3.2 ± 0.1	5.8 ± 0.2
T_1 (keV)	0.23 ± 0.06	0.24 ± 0.01	0.29 ± 0.01	0.24 ± 0.01
T_2 (keV)	0.69 ± 0.03	1.14 ± 0.1	2.0 ± 1.4	0.63 ± 0.02
EM_1 (10^{53} cm^{-3})	12.0 ± 5.0	18.8 ± 6.4	16.0 ± 4.2	17.2 ± 6.4
EM_2 (10^{53} cm^{-3})	0.96 ± 0.42	0.45 ± 0.12	0.14 ± 0.20	0.83 ± 0.42
flux ($10^{-12} \text{ erg cm}^{-2} \text{ s}^{-1}$)	1.01	0.89	0.99	0.92
O/O $_{\odot}$	0.13 ± 0.03	0.08 ± 0.02	0.08 ± 0.02	0.09 ± 0.02
Ne/Ne $_{\odot}$	0.18 ± 0.05	0.22 ± 0.06	0.16 ± 0.03	0.16 ± 0.03
Si/Si $_{\odot}$	0.72 ± 0.24	0.23 ± 0.13	0.40 ± 0.13	0.41 ± 0.16
Fe/Fe $_{\odot}$	0.45 ± 0.13	0.28 ± 0.08	0.17 ± 0.03	0.32 ± 0.08

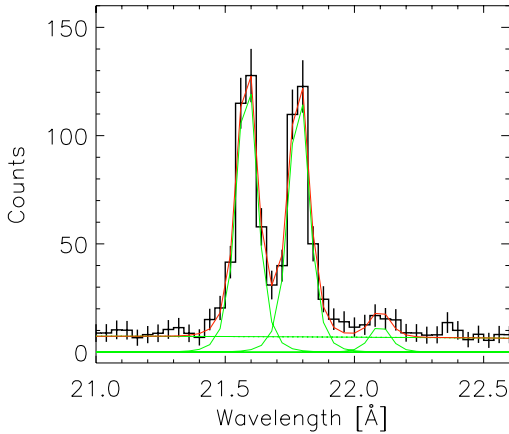


Fig. 8. The 4 coadded RGS1+RGS2 spectra in the region of the O VII triplet, with the fit to the 3 lines plus a constant.

the intercombination doublet i (which is blended into a single observed line) and the forbidden line f . The intensity ratio f/i is determined by both the plasma density (above a certain critical density which changes from element to element) and on the ambient UV field. The f line is the product of the decay from a metastable state; at low density and in the absence of an ambient radiation field the metastable state will decay undisturbed and the f line will be at maximum strength. Both collisions and radiative pumping can depopulate the metastable state, so that an increase in density or in the ambient radiation field will result in a less intense f line. For the triplets of interest, the radiative pumping depopulating the metastable state is due to ambient UV photons. While in cool stars the f/i ratio is commonly used as diagnostic of plasma density, in hot stars (such as β Cep) the ambient UV field due to the star's photospheric emission is strong and dominates the observed f/i ratio for the

typical plasma densities. The f/i ratio depends on density and UV field through the relation

$$R = R_0 \frac{1}{1 + \phi/\phi_c + n_e/n_c} \quad (3)$$

where R_0 is the f/i ratio in the limit of low-density and negligible UV field, n_e is the electron density of the plasma, n_c is the critical density (approximately, for N VI, 5×10^9 , for O VII 3×10^{10} and for Ne IX $6 \times 10^{11} \text{ cm}^{-3}$), ϕ is the UV photoexcitation rate of the relevant transition (which depends on the ambient UV radiation field due to the star's photospheric emission, at the wavelength of 1906, 1637 and 1270 Å respectively for N VI, O VII and Ne IX), and ϕ_c is the rate at which $R = R_0/2$. To determine the photoexcitation rate ϕ we have kept into account the variation of the UV flux with distance from the photosphere, using the formalism of Mewe & Schrijver (1978) who embed this effect in the so-called dilution factor.

Under the assumption that the plasma is below the critical density n_c , the observed f/i ratio depends only on the distance from the photosphere, and therefore the observed value can be used to indicate the characteristic distance at which the bulk of the emitting plasma is located. Given that the expected density from e.g. the MCWS model are below 10^9 cm^{-3} we expect this assumption to be verified.

We have performed the analysis of the 3 triplets visible in our spectra, namely N VI, O VII and Ne IX. The fluxes for all major lines used in our analysis are reported in Table 4. For the N VI triplet no forbidden line is detected in the spectrum. The upper limit to its flux translates into an upper limit on the f/i ratio and thus on the characteristic distance of the plasma from the photosphere.

The Ne IX triplet is significantly affected by blending, with the blending lines not resolved at XMM-Newton resolution. While the forbidden line is relatively isolated, the intercombination line is strongly affected by blending from Fe lines, which would require very high S/N and resolution to be properly resolved (e.g. Ness et al., 2003). In our spectra the f line is not

Table 4. The line fluxes measured in the RGS spectrum. Fluxes are in 10^{-6} photons $\text{cm}^{-2} \text{s}^{-1}$.

Det.	Line ID	λ	flux	error
RGS2	Ne x Ly α	12.132	10.6	1.7
RGS2	Ne ix r	13.447	10.4	1.7
RGS2	Ne ix i	13.550	8.8	1.7
RGS2	Ne ix f	13.700	1.6	0.9
RGS2	Fe xvii	15.010	21.7	2.2
RGS2	Fe xvii	15.190	6.1	1.4
RGS2	Fe xvii	15.260	8.9	1.6
RGS2	Fe xviii+O viii Ly β	16.010	6.6	1.9
RGS2	Fe xvii	16.070	3.6	1.9
RGS2	Fe xvii	16.780	17.7	2.0
RGS2	Fe xvii	17.050	20.8	3.1
RGS2	Fe xvii	17.096	18.9	3.0
RGS2	O vii	18.627	6.8	1.5
RGS2	O viii Ly α	18.970	59.4	3.2
RGS1	O vii r	21.600	45.1	3.4
RGS1	O vii i	21.800	41.3	3.2
RGS1	O vii f	22.100	4.8	1.9
RGS2	N vii Ly α	24.780	21.2	2.2
RGS2	N vi r	28.790	18.4	2.3
RGS2	N vi i	29.080	17.2	2.3
RGS2	N vi f	29.530	2.4	1.8

detected, again giving only an upper limit to the characteristic distance from the star.

In the O vii triplet the forbidden line is detected, at the $\approx 3\sigma$ level, in the coadded spectra (Fig. 8), resulting in a determination of the ratio $f/i = 0.095 \pm 0.033$.

To determine the influence of the photospheric UV flux on the X-ray triplets, a measure of the star's UV field is needed. The simplest approach is to use the star's effective temperature (26 000 K) and, under the assumption of a black body emitter, compute the resulting UV flux at the wavelength of interest. A more empirical approach relies on the measurement of the UV flux at the wavelengths of interest based on e.g. IUE spectra. We have compared the results obtained using both approaches.

To determine the UV flux at the 3 wavelengths of interest we have retrieved from the public archive an IUE observation of β Cep, from which the flux at Earth has been determined. To derive the radiation intensity at the stellar surface, the flux needs correcting for the effects of interstellar extinction. Extinction toward β Cep is modest, and the values in the literature range from $E_{B-V} = 0.04$ (Kontizas & Theodossiou, 1980) to $E_{B-V} = 0.01$ (Krelowski & Sneden, 1993). To assess the sensitivity of our analysis to the value of interstellar extinction we have considered both the case $E_{B-V} = 0.04$ and a case for no measurable extinction. Using the UV interstellar extinction law reported by Zombeck (1990) we have determined the extinction at each of the 3 wavelengths, determined the radiation intensity and derived the equivalent blackbody temperature.

The dependence of the f/i ratio on the distance from the star's photosphere is plotted in Fig. 9, for the three different assumptions regarding the photospheric UV flux (black body, IUE spectrum with $E_{B-V} = 0.00$, IUE spectrum with

Table 5. The unabsorbed UV flux at Earth and intensity at the stellar photosphere, at the wavelength relevant for the radiative pumping of the f transition for the N vi, O vii and Ne ix triplets, derived from an IUE spectrum of β Cep. F_λ in units of $\text{erg cm}^{-2} \text{s}^{-1} \text{\AA}^{-1}$, I_λ in units of $\text{erg cm}^{-2} \text{s}^{-1} \text{\AA}^{-1} \text{sr}^{-1}$

	E_{B-V}	N vi (1906 \AA)	O vii (1637 \AA)	Ne ix (1270 \AA)
F_λ	0.00	3.8×10^{-9}	5.6×10^{-9}	1.1×10^{-8}
I_λ	0.00	1.1×10^9	1.6×10^9	3.2×10^9
T	0.00	19 995	21 227	23 969
F_λ	0.04	5.1×10^{-9}	7.4×10^{-9}	1.6×10^{-8}
I_λ	0.04	1.5×10^9	2.1×10^9	4.6×10^9
T	0.04	21 674	22 701	25 899

$E_{B-V} = 0.04$). For each triplet the range of f/i determined from the observed spectrum is indicated by a thicker line. For N vi and Ne ix an upper limit to the location of the plasma can be determined, of respectively $\approx 15\text{--}25 R_\star$ for N vi and $\approx 2.5\text{--}3 R_\star$ for Ne ix, depending on the assumption for the UV field. In the following we adopt the curve derived using the UV flux determined from the IUE spectrum and $E_{B-V} = 0.04$.

For O vii the characteristic distance of the emitting plasma from the photosphere is between ≈ 3 and $\approx 5 R_\star$ using the UV flux determined from the IUE spectrum and $E_{B-V} = 0.04$. If the O vii emitting plasma is located at an effective distance from the photosphere of $\approx 5 R_\star$, the rotational velocity of the plasma, assuming rigid rotation at the star's rotational period of 12 d, would be 190 km/s, decreasing to 130 km/s for an effective distance of $\approx 4 R_\star$. Such velocity is below the velocity resolution of the *Chandra* LETG/HRC instrument, and therefore one expects (as indeed observed) that the spectral lines in the LETG spectrum will be consistent with the instrumental profile.

The RGS spectrum also allows to easily derive abundance ratios by taking the ratios of lines of different elements characterized by similar emissivities as a function of temperature (Drake & Testa, 2005). Using the Ne x Ly α at 12.132 \AA , Ne ix r line at 13.447 \AA and the O viii Ly α line at 18.970 \AA we have derived a ratio Ne/O of 0.32 ± 0.05 (about twice the solar ratio of 0.18 e.g. from Grevesse & Sauval, 1998), marginally consistent within the error bars with the ratio derived from the pn spectrum (≈ 0.67).

4.3. Chandra/LETG observations

The main aim of the *Chandra* LETG observation of β Cep was to study the X-ray line profiles at the highest possible spectral resolution for the low-temperature plasma of β Cep, with the aim of detecting either a modulation in the line centroid or a broadening in the line profile. In the MCWS scenario modulation in the line centroid in phase with the rotation period would be expected if the plasma is distributed non-homogeneously around the star and at sufficient distance from the star so that the rotational velocity is visible as Doppler shift.

If on the other hand the plasma is distributed uniformly, no velocity shifts are expected, but stellar rotation will induce a broadened line profile. Assuming for β Cep $R = 6.5 R_\odot$, and

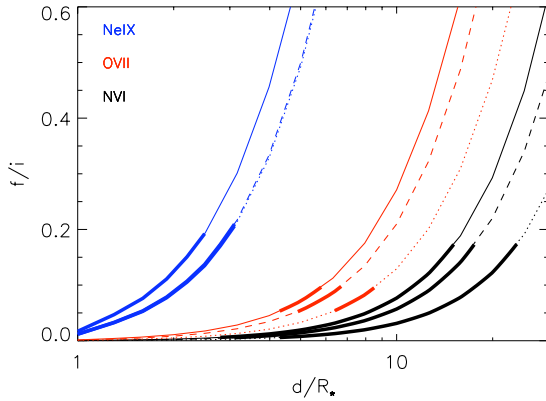


Fig. 9. The thick lines show the measured 1σ range for the f/i line ratios, and indicate the allowed distance for the location of the X-ray emitting plasma for the Ne IX, O VII and N VI triplets. The continuous curve corresponds to the UV flux determined from the IUE spectrum with $E_{B-V} = 0.00$, the dashed curve to the same with $E_{B-V} = 0.04$, and the dotted curve to the UV flux corresponding to a 26 000 K blackbody.

the rotational period of 12 d, the velocity of a plasma orbiting around the star will be $v = 28 \times r \text{ km sec}^{-1}$, where r is the distance of the plasma from the stellar center expressed in stellar radii.

For this purpose we obtained four *Chandra* observations of β Cep (ObsIDs 5395, 6138, 7194 and 7195) using the low energy transmission grating (LETG) with the high-resolution camera spectroscopic array (HRC-S). The phases spanned by the four *Chandra* exposures are listed in Table 6, computed using the ephemeris of D01. While the original plan was to obtain 4 observations at phases as close as possible to 0.0, 0.25, 0.5 and 0.75, the current restrictions on *Chandra* operations limited the accessible phases. As Table 6 shows, two datasets were taken near phase 0.0 and the final two observations were acquired near phase 0.25, providing a more limited phase sampling than originally planned, but still allowing to sample the system in both face-on and edge-on configurations. The resulting LETG spectrum, obtained by summing all the four observations together, is shown in Fig. 10.

The LETG/HRC-S configuration enables precise measurement of velocity shifts in X-ray spectra as the instrumental FWHM is 0.057 \AA , which corresponds to a velocity FWHM of approximately 900 km/s beyond a wavelength of 19 \AA . As shown e.g. by Hoogerwerf et al. (2004), the precision with which the centroid of a line profile can be measured depends strongly on the peak number of counts in the line profile. By summing up the counts obtained over two exposures centered around similar phases, we can maximise our centroiding ability. Given the count rate of β Cep, and the exposure times, our measurement error on the centroid position of the strongest unblended line profile, O VIII 18.97 \AA , for observations 1 and 2 (centered at phases 0.05 and 0.27 respectively) corresponds to $\sim 160 \text{ km/s}$.

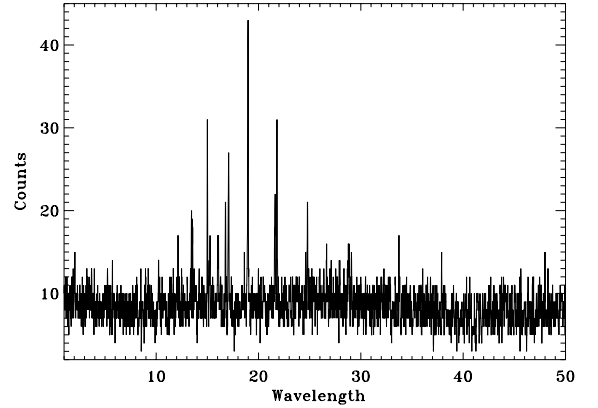


Fig. 10. The LETG spectrum of β Cep obtained by summing together the four *Chandra* observations discussed here.

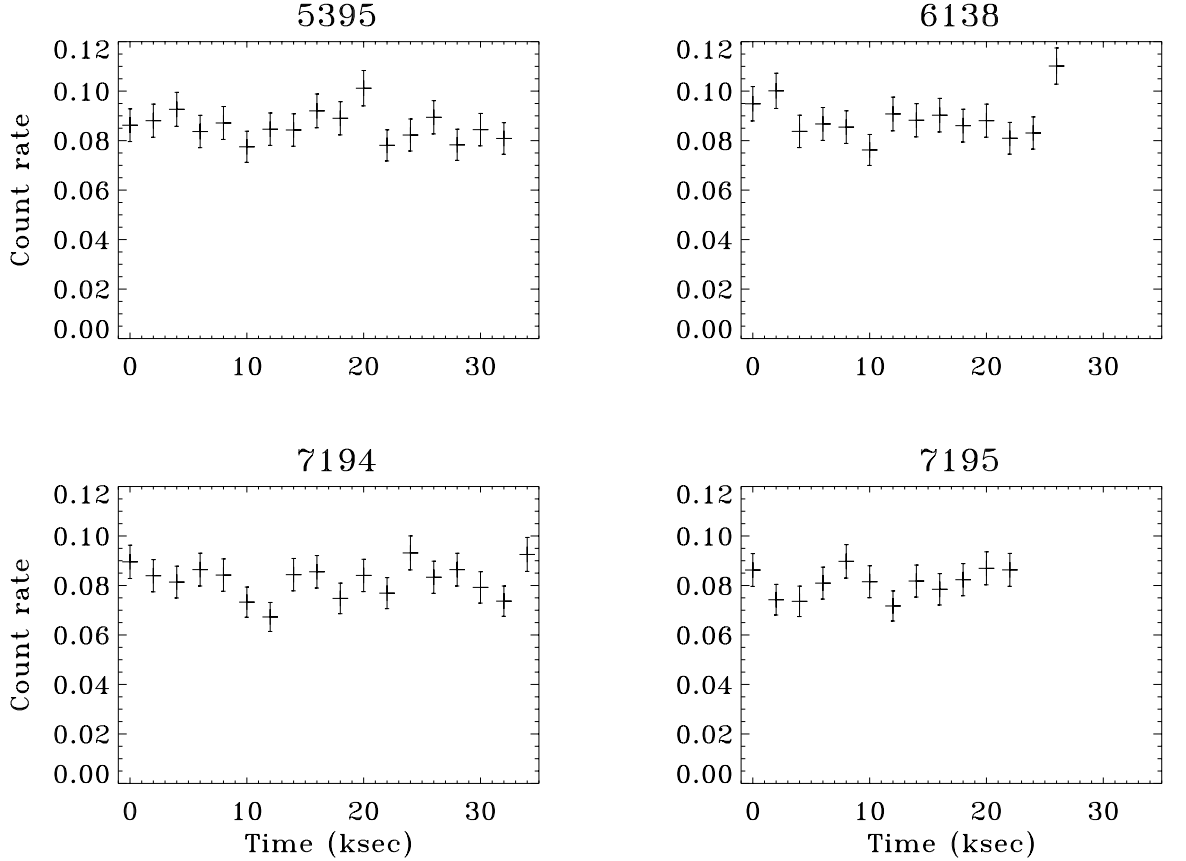
The spatial resolution of *Chandra* can easily resolve β Cep from its companion at 13.4 arcsec . Visual inspection of the *Chandra* image shows that no X-ray emission is visible from the companion, and that the X-ray source is coincident with the optical position of β Cep within a fraction of arcsec. The speckle companion at 0.1 arcsec is on the other hand not resolved.

We have first extracted the light curve of the *Chandra* observation, searching for evidence of rotational modulation of the X-ray emission. The 4 light curves for the 4 observations are plotted in Fig. 11. The emission is constant across the 4 segment, showing, similarly to the XMM-*Newton* observation, no evidence of rotationally modulated X-ray emission. No significant flaring is present, and no systematic changes in the X-ray flux are observed between the different observation phases.

We then searched for evidence of rotational modulation in the radial velocity of the emitting plasma by analyzing both the centroid and the profile of the 19 \AA O VIII line. Given the limited phase sampling afforded by the *Chandra* observations we again summed together the two observations close to phase 0.0 and the two observations close to phase 0.25. No evidence of varying Doppler shift with phase is present in our observations: as shown in Table 4.3, the position of the line centroid is constant, with no difference in the nominal position within the error estimate. The same applies to the line's FWHM.

As mentioned above, the strongest unblended line profile in the dataset is the O VIII resonance doublet near 18.97 \AA . Gaussian fitting procedures in the data analysis package *Sherpa* have been used to measure the centroid positions of the +1 and -1 order profiles. We find that any velocity shift in the line's centroid is the measurement errors (see Table 4.3). We conclude, therefore, that there is no measurable change in the radial velocity of the X-ray emitting plasma. Given the measurement errors of 0.01 \AA we put an upper limit to any relative velocity shifts of $\leq 160 \text{ km/s}$ when comparing spectra centered at phases 0.05 and 0.27. Furthermore, the O VIII 18.97 \AA line width is consistent with the instrumental broadening, which has a FWHM = 900 km/s (Table 4.3).

ObsID	Exposure ksec	T_{start} JD	T_{end} JD	ϕ_{start}	ϕ_{end}	Count rate cts/sec
5395	36.43	2 453 674.4519389	2 453 674.8897456	0.0096	0.0461	0.086
6138	29.54	2 453 675.0851294	2 453 675.4490259	0.0624	0.0927	0.089
7194	38.17	2 453 677.1208892	2 453 677.5798238	0.2320	0.2702	0.082
7195	27.15	2 453 677.7494105	2 453 678.0855105	0.2844	0.3124	0.075

Table 6. The observation log of the *Chandra* data sets.**Fig. 11.** The light curve of the 4 *Chandra* observations, integrated at 2 ks binning. No evidence of modulation with the rotational period is present.

Mean ϕ	$\lambda_o (-1)$ [Å]	$\lambda_o (+1)$ [Å]
0.05	18.976 ± 0.010	18.970 ± 0.010
0.27	18.971 ± 0.009	18.977 ± 0.006
	FWHM (-1) [Å]	FWHM (+1) [Å]
0.05	0.07 ± 0.03	0.06 ± 0.03
0.27	0.05 ± 0.01	0.05 ± 0.02

Table 7. The mean wavelength and FWHM of the O VIII line, grouping observations in two groups of two, maximizing the phase sampling.

In order to investigate the level of broadening in the emission line profiles, we summed up the counts from the strongest line profiles in the spectral dataset. The strongest six line profiles all showed peaks with more than 15 counts; these were used to build a composite profile to investigate the origin of

the X-ray emission from the system. This profile is built by first measuring the zero-velocity positions of the line profiles using the entire spectrum computed by summing over all four exposures. This is valid as the source position remains within 1 or 2 pixels between all observations; hence the wavelength scale should be consistent between all four pointings. After the zero-velocity positions are established, both the +1 and -1 order spectra are converted to velocity-space using these zero-velocity offsets; they are then interpolated to the same wavelength resolution (187 km/s or 0.0125 Å), which corresponds to a line at the mean wavelength (20 Å) and co-added. The wavelengths of the lines used are centered at: Fe XVII 15.014 Å, Fe XVII 17.0510 Å, O VIII 18.9725 Å, Fe XVII 21.6015 Å, O VII 21.8036 Å and N VI 24.7792 Å respectively.

Figure 12 shows the composite profiles for orders ± 1 compared to the combined instrumental profile for the six strongest

lines (dashed line). This was produced by scaling the instrumental profile until it fitted the amplitude of the corresponding strong line for each of the six strong line profiles; interpolating the scaled instrumental profile to the same velocity scale used for the composite profile and co-adding all of these scaled, interpolated instrumental profiles to produce a composite instrumental profile. A similar analysis performed on phase-grouped spectra also failed to reveal any change in the line profile and positions.

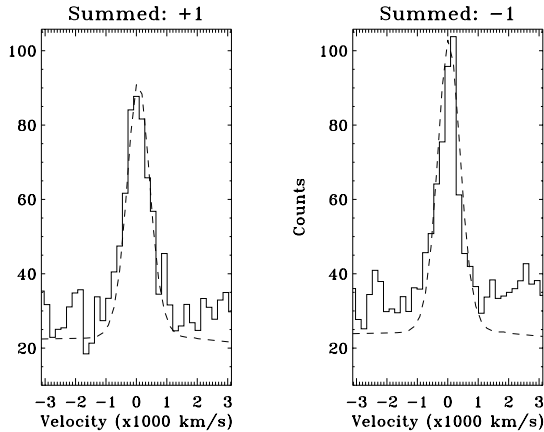


Fig. 13. The summed line profiles obtained adding up the Fe xvii 15.014 Å, Fe xvii 17.0510 Å, O viii 18.9725 Å, O vii 21.6015 Å, O vii 21.8036 Å and N vi 24.7792 Å lines from the 4 *Chandra* observations. The dotted line shows the composite instrumental profile.

We then analyzed the individual line profiles for evidence of velocity broadening, looking at both the line profiles from the individual observations (Fig. 12) as well as to the line profile obtained by summing all strong lines (Fe xvii 15.014 Å, Fe xvii 17.0510 Å, O viii 18.9725 Å, O vii 21.6015 Å, O vii 21.8036 Å and N vi 24.7792 Å) from all 4 observations. This allows (in the hypothesis of no variability from one observation to the other) to obtain a much higher S/N and thus to determine the line profile to a higher accuracy. In fact, all the observed lines are consistent with the instrumental resolution ($\Delta\lambda \approx 0.05$ Å for the LETG/HRC instrumental combination), and thus allow us to exclude the presence of plasma moving at velocities ≥ 600 km s $^{-1}$. In the case of rotational broadening this translates to a maximum distance from the stellar center $d \lesssim 20 R_*$. While not very constraining, this provides an upper limit to the distance of the X-ray emitting plasma, which, in conjunction with the lower limits provided by the He-like triplet analysis, allows to bound the location of the X-ray emitting region around the star.

The terminal wind velocity of β Cep has been estimated between 800 km/s (D01) and 1500 km/s (Schnerr et al., 2007); the lack of observed broadening points toward X-ray emission from a magnetically confined plasma, rather than from a freely flowing wind.

We also verified that the f/i ratios in the LETG spectra are consistent with the values derived for the RGS spectra.

However, given their lower S/N the LETG f/i ratios have significantly larger associated uncertainties and thus do not help in further constraining e.g. the location of the plasma.

5. Discussion and conclusions

5.1. X-ray modulation and location of the plasma

β Cep has a close B6-8 companion which could be the component on which the H α emission is located (Schnerr et al., 2006). The companion is very unlikely to be contributing to X-ray emission in the β Cep system: in the regime in which X-ray emission is originating in shocks in the wind (i.e. for OB stars) the emission increases with stellar mass and spectral type; therefore the B1 primary is very likely dominating the X-ray emission from the system and thus all our conclusions are unaffected by the presence of the late B-type companion and by the fact that the β Cep primary may no longer be considered a Be star.

Our X-ray campaign on β Cep shows limited evidence of modulation of its X-ray emission level, both short-term (i.e. within a rotational period) and long-term (i.e. from one observation to the other), with for example the ROSAT and XMM-Newton observations showing very similar flux levels across several years. Evidence of low-level modulation of the X-ray emission with stellar rotation is present in the pn low-resolution X-ray data, while the LETG and RGS high-resolution spectra appear remarkably similar to each other. For instance, as shown in Fig. 7, the O vii triplet shows no evidence of variation from one rotational phase to the other. For the *Chandra* LETG spectra little if any variability is present in the line fluxes as well as in the centroid of the line positions.

Such high degree of constancy in the X-ray emission is in contradiction with the high ($\approx 50\%$) level of rotational modulation expected in the MCWS framework of D01: with the geometry of β Cep the disk is seen alternatively face-on and edge-on. If indeed X-ray emission is due to stationary shocks on either side of the disk (which is expected to have a high optical thickness at soft X-ray wavelengths), during face-on configurations about 50% of the flux should be absorbed.

In contrast to what was expected from the MCWS scenario by D01, we find a slightly ($\approx 10\%$) higher emission level for the face-on configuration with respect to the edge-on configuration. This allows us to exclude the simple scenario proposed by D01 and in particular it definitively rules out the presence of the optically thick layer in the magnetic equator. Such smaller modulation, with the observed phase, is along the lines predicted by the dynamical MCWS models of ud-Doula & Owocki (2002) and Gagné et al. (2005), which would indeed predict for the β Cep configuration, no thick disk and a modulation of approximately 5%, fully consistent with the observed values.

The measurements of the line intensity in the He-like triplets, and in particular the O vii one, allows us to determine the location of the bulk of the emitting plasma. The temperature of formation of the O vii triplet peaks at 0.17 keV, not very different from the characteristic temperature of the bulk of the emitting plasma, as determined from the pn spectra. Therefore, the characteristic distance from the star's photosphere deter-

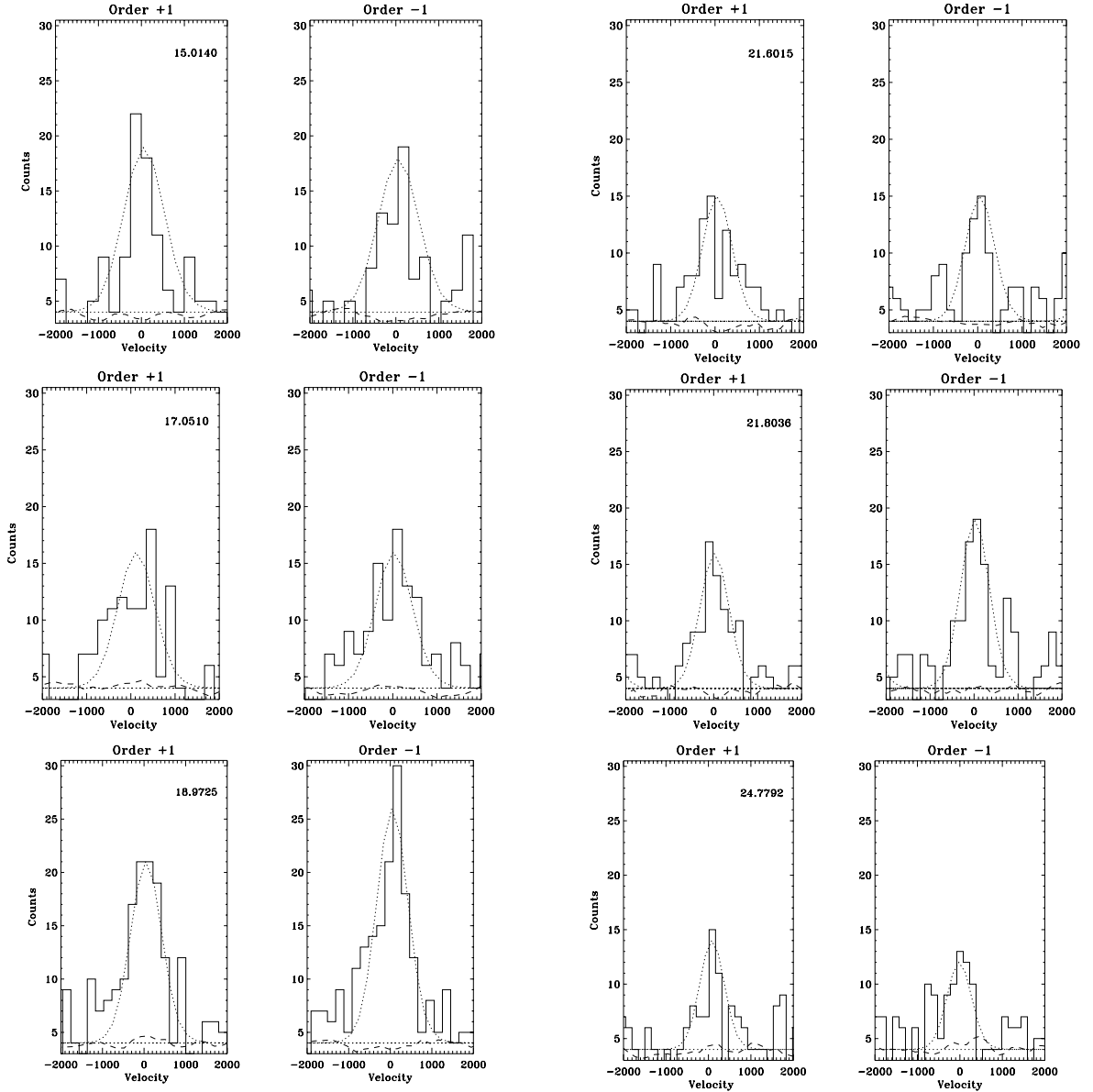


Fig. 12. The line profiles for the Fe xvii 15.014 Å, Fe xvii 17.0510 Å, O viii 18.9725 Å, O vii 21.6015 Å, O vii 21.8036 Å and N vi 24.7792 Å lines respectively, obtained by adding all 4 *Chandra* observations.

mined from the O vii triplet should be representative of the majority of the plasma at X-ray temperatures. The detection at $\sim 3\sigma$ of the f line in the O vii triplet allows us to determine a distance range from the photosphere (rather than an upper limit), estimated to be $d \simeq 4R_*$ (see sec. 4.2). The derived location for the X-ray emitting plasma is also consistent with the location predicted by the ud-Doula & Owocki (2002) and Gagné et al. (2005) models, which locate the plasma between the Alfven and Kepler radii, i.e. between $R \simeq 5R_*$ and $R \simeq 7R_*$.

An additional constraint on the spatial location of the X-ray plasma in β Cep comes from the relation between the plasma pressure and the confining magnetic field, under the assumption that the X-ray emitting plasma is indeed magnetically confined, in agreement with the lack of line broadening otherwise

expected for a standard wind shock model. The plasma density can be derived from the emission measure, derived either from the global fit to the pn spectrum, or taking the emission in a given line. If we take the flux in the strongest (r) O vii line, we derive $EM = 1.5 \times 10^{55} \text{ cm}^{-3}$. Assuming the plasma to be confined in a spherical shell comprised between 4 and $6R_*$ (as derived from the triplet ratios), the emitting volume is $V = 7.5 \times 10^{37} \text{ cm}^3$, resulting in an average plasma density $n = 4.5 \times 10^8 \text{ cm}^{-3}$. Such low density is consistent with no density effect on the He-like triplets of the elements being considered. The magnetic field needed to confine this plasma (taking into account the average temperature $T \simeq 0.3 \text{ keV}$) is $B = \sqrt{8\pi 2nkT} \simeq 3 \text{ G}$. Assuming the stellar magnetic field to be dipolar, and taking the best estimate for the polar magnetic field of 355 G, and scaling the dipolar field as d^3 (d being the dis-

tance from the star), the magnetic field at $5 R_\star$ from the photosphere is $355/5^3 \approx 3$ G, similar to the pressure required to confine the emitting plasma. This indicates that the emitting plasma is weakly confined by the magnetic field, with $\beta \approx 1$.

Using the location of the plasma found above ($R_{\text{out}} = 6 R_\star$ and $R_{\text{in}} = 4 R_\star$) and assuming a geometrically thin disk, we can estimate the variation of the X-ray flux from edge-on to face-on configuration to be of the order of 7%. This number is compatible within the error bars with the observed variation level. This scenario would rule out the presence of X-ray emitting plasma at high latitudes above the magnetic equator and is again compatible with the predictions from the more recent, dynamical MCWS models.

5.2. Magnetic confinement

Standard models of X-ray emission from massive stars, originating in shocks in an unconfined wind, predict both a general blue-shifting of the line together with its broadening. The magnitude of the expected broadening is comparable with the wind terminal velocity, which in the case of β Cep is $\approx 800 - 1500$ km/s. The blue-shift depends on the amount of absorption of the line's red wing, and is expected to be less than the broadening.

The analysis of the LETG line profiles rule out the presence of any broadening above the instrumental line profile, which has a FWHM of approximately 600 km/s, and of blue-shifts greater than 160 km/s. While they are not extremely constraining relative to the wind terminal velocity of β Cep, these elements indicate a lack of any significant bulk motions in the X-ray emitting plasma, and point toward its being magnetically confined, therefore ruling out, for β Cep, X-ray emission from shocks in an unconfined wind.

The relatively low temperature of the X-ray emitting plasma (with the dominant component being at ≈ 3 MK) together with the lack of significant short-term variability (flares) point however to a lack of magnetic heating (i.e. due to magnetic reconnection): in active cool stars, the magnetic reconnection that dominates the heating of the plasma results in much higher temperatures and stochastic variability. The high temperatures observed for θ^1 Ori C also points to the presence of magnetic heating in some massive stars.

In the case of β Cep the magnetic heating only has the apparent function of confining the plasma, which is likely heated to the observed 3 MK by shocks. Also, the bulk of the X-ray plasma appears to be confined by a relatively weak magnetic field, close to the limit where the magnetic pressure becomes too weak to confine the plasma.

5.3. Comparison with other stars

The behavior of β Cep as observed in our *Chandra* and XMM-*Newton* observations appears to be significantly different from the other well studied example of magnetically confined wind in a massive star, θ^1 Ori C. In that case, the X-ray emission is strongly modulated at the rotational period, by approximately 50%, as predicted by the MCWS model. At the same time, the

observed plasma temperatures are, for θ^1 Ori C, much higher than for β Cep, reaching up to 30 MK. Furthermore, the analysis of the triplets in θ^1 Ori C show that the emitting plasma is located much closer to the star's photosphere than in the case of β Cep. In θ^1 Ori C the bulk of the plasma is located at $\approx 1.5 R_\star$ while in β Cep the cooler plasma traced by the O triplet is located at $\approx 5 R_\star$, while the hotter plasma traced by the Ne triplet is located at $\lesssim 2 R_\star$ from the photosphere, pointing also to a stratification of the plasma as a function of temperature. Finally, the metal abundances determined for the θ^1 Ori C plasma are much higher than for β Cep. In β Cep all elements appear to be depleted with the exception of Si, while many elements are enhanced in the θ^1 Ori C spectrum, showing a different process in operation.

Gagné et al. (2005) have modeled the observed emission from θ^1 Ori C with a dynamic version of the MCWS, showing that both infall to the photosphere and outflow make it unlikely that the thick disk predicted by Babel & Montmerle (1997a) would actually form. They interpret the observed modulation (which goes in the opposite direction from the one predicted by the D01 model, as also observed by us for β Cep) as occultation of the X-ray emitting plasma (located, in their model, close to the equator) by the stellar photosphere.

A similar situation, with the dynamics preventing the thick disk from forming, is possibly present in β Cep, so that also in this case the X-ray emission is produced by a magnetically confined wind, with the lower observed temperatures explained by the lower wind velocity.

5.4. Conclusions

The *Chandra* and XMM-*Newton* observations discussed here have failed to display the signatures expected by the static MCWS model of D01, in particular the strong rotational modulation of the X-ray emission due to the presence of the cool disk around the star. However the X-ray plasma appears confined, and a small amplitude modulation is visible in the XMM-*Newton* EPIC data. Together with the low temperature and the lack of flaring, this can be interpreted as emission from a magnetically confined wind but without the cool, optically thick disk predicted by the D01 model. The observed modulation is fully compatible with the emission scenario predicted by the more recent dynamical MCWS models for a star with the characteristics of β Cep.

Acknowledgements. The authors thank the XMM-*Newton* and *Chandra* observatories for their support in the scheduling of a complex phase locked observation. Also the support of L. Scelsi in the analysis of the XMM-*Newton* RGS data is gratefully acknowledged. The authors also thank the referee, M. Gagne, for a very detailed and useful report.

References

- Abt, H. A., Levato, H., & Grosso, M. 2002, ApJ, 573, 359
- Agrawal, P. C., Singh, K. P., Riegler, G. R., & Stern, R. A. 1984, MNRAS, 208, 845
- Asplund, M., Grevesse, N., & Sauval, A. J. 2005, in ASP Conf. Ser. 336: Cosmic Abundances as Records of Stellar

- Evolution and Nucleosynthesis, ed. T. G. Barnes, III & F. N. Bash, 25
- Babel, J. & Montmerle, T. 1997a, *ApJ*, 485, L29
- Babel, J. & Montmerle, T. 1997b, *A&A*, 323, 121
- Berghoefer, T. W., Schmitt, J. H. M. M., & Cassinelli, J. P. 1996, *A&AS*, 118, 481
- Cassinelli, J. P., Miller, N. A., Waldron, W. L., MacFarlane, J. J., & Cohen, D. H. 2001, *ApJ*, 554, L55
- Chung, S. M., Drake, J. J., Kashyap, V. L., Ratzlaff, P. W., & Wargelin, B. J. 2004, in *UV and Gamma-Ray Space Telescope Systems*, ed. G. Hasinger & M. J. L. Turner, Vol. 5488, 51
- Cohen, D. H. 2000, in *Astronomical Society of the Pacific Conference Series*, Vol. 214, IAU Colloq. 175: The Be Phenomenon in Early-Type Stars, ed. M. A. Smith, H. F. Henrichs, & J. Fabregat, 156
- Cohen, D. H., Leutenegger, M. A., Grizzard, K. T., et al. 2006, *MNRAS*, 368, 1905
- Cugier, H. & Boratyn, D. A. 1992, *Acta Astronomica*, 42, 191
- Daszyńska-Daszkiewicz, J. & Niemczura, E. 2005, *A&A*, 433, 1031
- Donati, J.-F., Babel, J., Harries, T. J., et al. 2002, *MNRAS*, 333, 55
- Donati, J.-F., Howarth, I. D., Bouret, J.-C., et al. 2006, *MNRAS*, 365, L6
- Donati, J.-F., Wade, G. A., Babel, J., et al. 2001, *MNRAS*, 326, 1265
- Drake, J. J. & Testa, P. 2005, *Nat*, 436, 525
- Dziembowski, W. A. & Pamiatnykh, A. A. 1993, *MNRAS*, 262, 204
- Gagne, M., Caillault, J.-P., Stauffer, J. R., & Linsky, J. L. 1997, *ApJ*, 478, L87
- Gagné, M., Oksala, M. E., Cohen, D. H., et al. 2005, *ApJ*, 628, 986
- Gezari, D. Y., Labeyrie, A., & Stachnik, R. V. 1972, *ApJ*, 173, L1
- Grevesse, N. & Sauval, A. J. 1998, *Space Science Reviews*, 85, 161
- Henrichs, H. F., de Jong, J. A., Donati, D.-F., et al. 2000, in *Magnetic Fields of Chemically Peculiar and Related Stars*, ed. Y. V. Glagolevskij & I. I. Romanyuk, 57
- Henrichs, H. F., Schnerr, R. S., & Ten Kulve, E. 2005, in *ASP Conf. Ser. 337: The Nature and Evolution of Disks Around Hot Stars*, ed. R. Ignace & K. G. Gayley, 114
- Heynderickx, D., Waelkens, C., & Smeyers, P. 1994, *A&AS*, 105, 447
- Hoogerwerf, R., Brickhouse, N. S., & Mauche, C. W. 2004, *ApJ*, 610, 411
- Hutchings, J. B. & Hill, G. 1977, *ApJ*, 213, 111
- Kashyap, V. & Drake, J. J. 2002, in *Astronomical Society of the Pacific Conference Series*, Vol. 277, *Stellar Coronae in the Chandra and XMM-NEWTON Era*, ed. F. Favata & J. J. Drake, 509
- Kontizas, E. & Theodossiou, E. 1980, *MNRAS*, 192, 745
- Krelowski, J. & Sneden, C. 1993, *PASP*, 105, 1141
- Leutenegger, M. A., Paerels, F. B. S., Kahn, S. M., & Cohen, D. H. 2006, *ApJ*, 650, 1096
- Lucy, L. B. & White, R. L. 1980, *ApJ*, 241, 300
- Mewe, R. & Schrijver, J. 1978, *A&A*, 65, 99
- Morel, T., Butler, K., Aerts, C., Neiner, C., & Briquet, M. 2006, *A&A*, 457, 651
- Ness, J.-U., Brickhouse, N. S., Drake, J. J., & Huenemoerder, D. P. 2003, *ApJ*, 598, 1277
- Niemczura, E. & Daszyńska-Daszkiewicz, J. 2005, *A&A*, 433, 659
- Pan'ko, E. A. & Tarasov, A. E. 1997, *Astronomy Letters*, 23, 545
- Pigulski, A. & Boratyn, D. A. 1992, *A&A*, 253, 178
- Schnerr, R. S., Henrichs, H. F., Oudmaijer, R. D., & Telting, J. H. 2006, *A&A*, 459, L21
- Schnerr, R. S., Henrichs, H. F., Owocki, S. P., Ud-Doula, A., & Townsend, R. H. D. 2007, in *Astronomical Society of the Pacific Conference Series*, Vol. 361, *Active OB-Stars: Laboratories for Stellar and Circumstellar Physics*, ed. A. T. Okazaki, S. P. Owocki, & S. Stefl, 488
- Schulz, N. S., Canizares, C., Huenemoerder, D., & Tibbets, K. 2003, *ApJ*, 595, 365
- Schulz, N. S., Testa, P., Huenemoerder, D. P., Ishibashi, K., & Canizares, C. R. 2006, *ApJ*, 653, 636
- Stelzer, B., Flaccomio, E., Montmerle, T., et al. 2005, *ApJS*, 160, 557
- Stibbs, D. W. N. 1950, *MNRAS*, 110, 395
- Tian, B., Men, H., Deng, L.-C., Xiong, D.-R., & Cao, H.-L. 2003, *Chinese Journal of Astronomy and Astrophysics*, 3, 125
- Townsend, R. H. D. & Owocki, S. P. 2005, *MNRAS*, 357, 251
- ud-Doula, A. & Owocki, S. P. 2002, *ApJ*, 576, 413
- Vaiana, G., Cassinelli, J., Fabbiano, G., et al. 1981, *ApJ*, 244, 163
- Waldron, W. L. & Cassinelli, J. P. 2007, *ApJ*, 668, 456
- Zombeck, M. 1990, *Handbook of Space Astronomy & Astrophysics*, 2nd ed. (Cambridge Univ. Press)